

# Characterization of High-Strength Weld Metal Containing Mg-Bearing Inclusions

*Microstructural analysis of flux cored welds using a 4% Ni steel consumable exhibits both high strength and toughness*

BY A. P. GERLICH, H. IZADI, J. BUNDY, and P. F. MENDEZ

## ABSTRACT

Weld metal deposited by flux cored arc welding that exhibited a combination of high strength and toughness was studied. Microstructural characterization revealed it contained primarily bainitic ferrite with a fine packet size in the as-deposited metal and mainly nonaligned ferrite in the reheated zones, which were concentrated near the root of the weld. A new type of spherical inclusion is reported with an average size of 311 nm in diameter that exhibits a shelled structure mainly rich in Al, Mg, and O in the core, and Mg, O in the outer shell. It is suggested the good properties stem from a combination of fine inclusion size, low content of interstitials, and small ferrite packet size. Instrumented impact testing indicates that grain refinement in reheated zones near the root of the weld improve the Charpy impact energy; however, fracture initiation energy is similar to the top of the weld.

sumables to achieve the desired acicular ferrite microstructure depending on these chemistry additions in the electrode. However, recent developments have shown that excellent toughness and strength may also be achieved with a complex combination of ferrite with martensite/austenite islands, martensite, degenerated pearlite, and upper bainite (Ref. 18). High-toughness weld metals based on large fractions of ferrite with nonaligned second phase and little acicular ferrite microconstituents were produced; however, this was limited to a tensile strength of 480 to 651 MPa (Ref.19). Alternative microstructures are of interest since they may offer reduced levels of interstitial oxygen and nitrogen, which will help to improve low-temperature toughness; however, these elements are normally required in forming inclusions that nucleate acicular ferrite.

The general consensus is that toughness during impact testing is limited in the upper shelf region by the volume fraction of nonmetallic inclusions, and by the type and morphology of microconstituents during brittle fracture in the lower shelf (Refs. 2, 20, 21). Since a ferrite structure with aligned second phase dominates at low-oxygen contents, the toughness is limited by the larger unit crack length path during brittle fracture (Refs. 22–24). Weld metal deposits that achieve Charpy impact energy values of 300 J at  $-50^{\circ}\text{C}$  (Ref. 25) are possible through optimizing oxygen and Ti content to control the formation of  $\text{TiO}_2$ , which nucleates acicular ferrite. However, there are a few techniques discussed that do not rely on acicular ferrite structures and do not use Ti additions.

This investigation examines the use of a flux cored arc welding consumable with a nominal tensile strength of more than 825 MPa, which does not utilize Ti additions or promote acicular ferrite formation. The weld metal can be deposited with 100%  $\text{CO}_2$  shielding gas, while containing low interstitial content with good low-tempera-

## Introduction

This research focuses on the use of a novel flux-cored arc welding wire formulation, which appears to depart from the typical mechanisms of microstructural development, resulting in outstanding weld metal strength and toughness. The traditional strategy for achieving a combination of high strength along with good low-temperature toughness in high-strength weld metals is to promote an acicular ferrite microstructure (Refs. 1–4). This microstructure consists of fine interlocking ferrite needles, with high grain boundary misorientations to promote grain boundary strengthening together with crack deviation during cleavage fracture at low temperatures (Refs. 5, 6). The nucleation of acicular ferrite occurs intragranularly in austenite on inclusions, and commercial weld consumables rely on Ti and Al additions to form inclusions such as  $\text{TiO}_x$ ,  $\text{TiN}$ , and  $\text{MnO}\cdot\text{Al}_2\text{O}_3$  (Refs. 7–9). The nucleation of acicular ferrite depends on achieving a large volume fraction of inclusions

with a diameter between 0.2 and 2  $\mu\text{m}$ , where the ideal size is close to 0.4  $\mu\text{m}$  (Refs. 10–13). It has been shown that achieving this structure typically occurs when the weld metal oxygen content is close to 200 ppm, where lower oxygen concentrations fail to produce the acicular ferrite, while higher values form excessive amounts of large oxide inclusions that are  $> 1 \mu\text{m}$  in diameter and nucleate cracks (Refs. 14, 15) and deteriorate toughness (Ref. 16).

Considering the influence of chemistry and cooling rate on the thermodynamics and kinetics of inclusion formation (Ref. 17), successful application of welding consumables using Ti additions requires careful control of welding parameters that influence the chemistry in the weld pool, particularly Ti, O, and N content. This can limit the operating window for some con-

## KEYWORDS

Flux Cored  
Microstructure  
Phase Formation  
Oxide Inclusions  
Instrumented Charpy  
Magnesium

A. P. GERLICH is with University of Waterloo, Mechanical and Mechatronics Engineering, Waterloo, Ontario, Canada, H. IZADI and P. F. MENDEZ are with University of Alberta, Chemical and Materials Engineering, Edmonton, Alberta, Canada, J. BUNDY is with Hobart Brothers, Troy, Ohio.

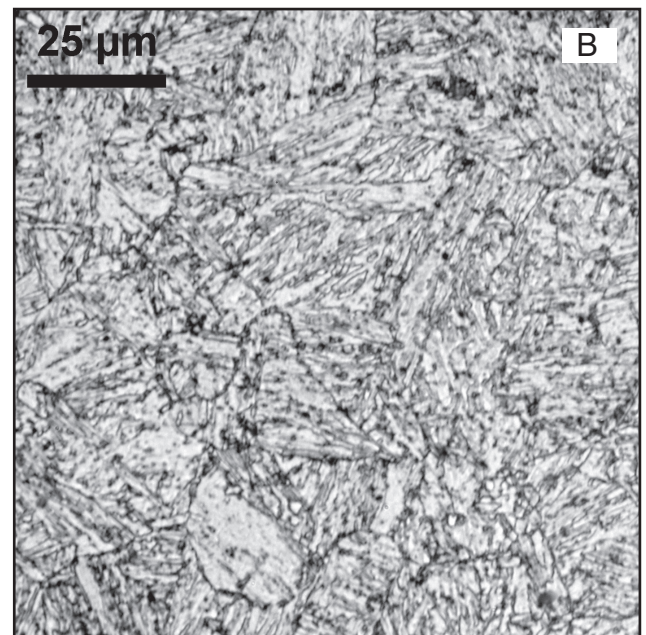
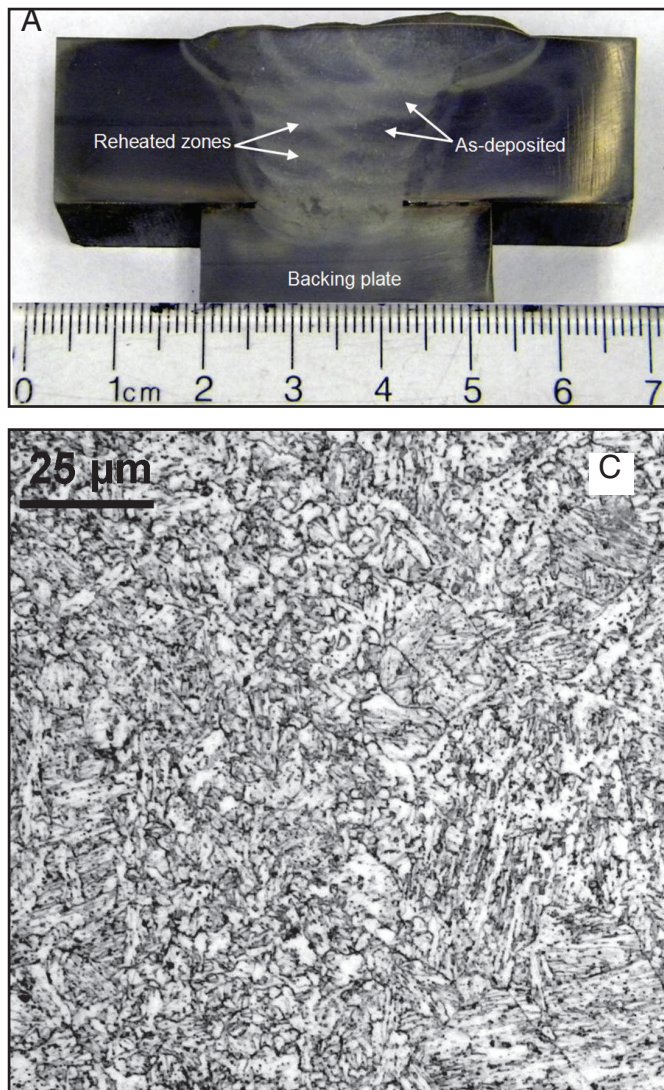


Fig. 1 — A — Macroscopic section of the joint; B — optical micrograph of the as-deposited weld metal; C — optical micrograph of the reheated weld metal.

ture toughness, as well as high strength. The microconstituents and inclusions are examined using a combination of optical and SEM microscopy, and the fracture properties are studied using instrumented impact testing followed by fractography.

### Experimental

The weld metal chemistry is summarized in Table 1, and has a calculated  $CE_{IIW}$  carbon equivalent of 0.62, and  $P_{cm}$  value of 0.21 (Ref. 26). The welds were completed using a flux cored arc welding (FCAW) consumable that conforms to AWS specification A5.29, with  $CO_2$  shielding gas, using

a current of 200 A, voltage of 24 V in direct current electrode negative (DCEN) polarity, and 0.0625-in. (1.6 mm) wire with a feeding rate of 200 in./min (84 mm/s). The details of the consumable design and flux chemistry have been reported elsewhere; however, it should be noted that the flux contains  $MgO$ , which provides an opportunity to introduce Mg content into the weld metal (Ref. 27). Welding was conducted in the flat (1G) position on a 0.75-in.-thick ASTM A514 steel plate with a 45-deg bevel angle, a 0.5-in. root opening and a backing plate, similar to other studies (Ref. 28). The travel speed was approximately 8 in./min during each welding pass, and the heat input was an average of 1.8 kJ/mm. During welding, the preheat or interpass temperature was 350°F (177°C), and no postweld heat treatment was applied.

Charpy impact testing was conducted between  $-73^\circ$  to  $20^\circ C$  on material ex-

tracted from the middle of the weld region. Additional welds were produced on a 75-mm-thick plate using the same conditions as above in order to facilitate extraction of  $10 \times 10$  mm Charpy coupons along the transverse direction of the weld. These were obtained from approximately 2 mm below the surface of the root, as well as 2 mm below the surface of the crown of the weld, in order to obtain mainly reheated or as-deposited weld metal, respectively, from these two regions. These top and bottom portions of the weld were also tested by instrumented impact testing in which the force and displacement were recorded during impact. Instrumented impact testing was used in order to provide a comparison of the relative fracture initiation energy values in these top and bottom regions of the weld.

The microstructures were analyzed using a combination of optical and SEM microscopy after etching with 2% nital. Microhardness indentation was used to determine the hardness of the reheated and as-deposited material. In order to determine the chemistry of fine inclusions, Auger electron spectroscopy (AES) was used to map elemental distributions. Further analysis of the inclusions was also conducted by

Table 1 — Weld Metal Chemistry (wt-%, balance Fe)

C	Mn	P	S	Si	Cu	Cr	V	Ni	Mo	Al	Ti
0.059	1.219	0.006	0.003	0.123	0.044	0.264	0.005	3.511	0.212	0.557	0.002
Nb	Co	B	W	Sn	Pb	Zr	Ce	As	O	N	Mg
0.003	0.005	0.0005	0.005	0.005	0.001	0.028	0.001	0.0034	0.012	0.0064	0.03

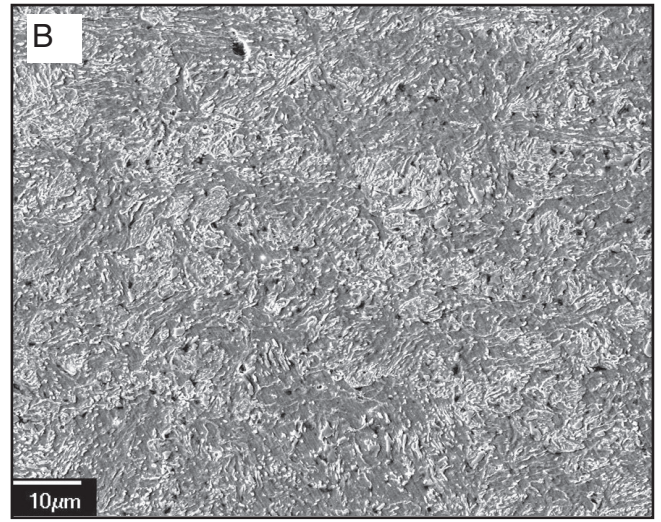
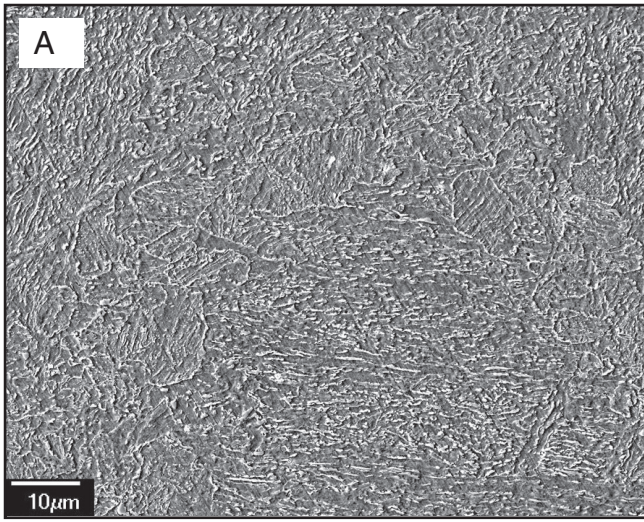


Fig. 2— SEM micrographs. A — As-deposited; B — reheated weld metal.

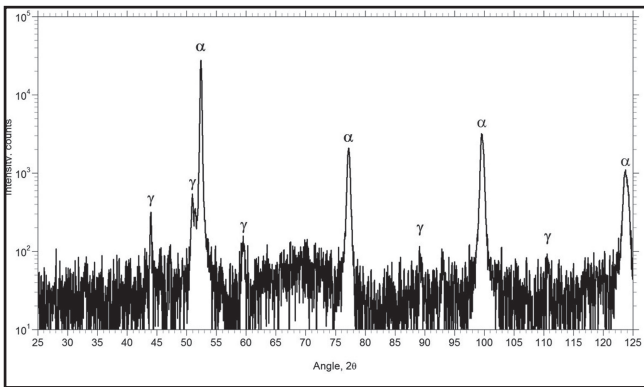


Fig. 3 — XRD spectrum of weld metal indicating presence of ferrite ( $\alpha$ ) and retained austenite ( $\gamma$ ).

dissolving the weld metal in a 25% HCl and 25% HNO<sub>3</sub> mixture, followed by collection of the dissolved metal residue on filter paper. The residue as well as the bulk weld metal was examined by XRD analysis. The weld metal solidification was also simulated by calculating the Scheil diagram using *ThermoCalc* version S with the TCFE6 database. The *ThermoCalc* investigations examined the chemistry shown in Table 1 for only elements >0.1 wt-% as well as oxygen and carbon, and the stability of all phases within the TCFE6 database. The algorithm for this is included within *ThermoCalc*, where the equilibrium composition of solid phases are calculated, assuming negligible diffusion in the solid and perfect mixing in the liquid.

while the upper region capping passes comprise mainly as-deposited material.

The weld metal mainly consisted of upper bainite, referred to as FS(A) microstructures in the as-deposited material, and bainitic ferrite or an FS(NA) microstructure in the reheated zones containing fine-grained material. These microstructures were identified using the modified IIW classification scheme (Ref. 29) as either ferrite with aligned second phase (FS(A)), ferrite with nonaligned second phases (FS(NA)), and polygonal ferrite (PF). Both the as-deposited and reheated weld metals were examined, and the area fractions of each of the ferrite morphologies or microconstituents were quantified by image analysis, summarized

Table 2 — Quantification of Ferrite Microstructures

Region, % Area Fraction	FS(A)	FS(NA)	PF
As deposited	82.4	17.2	0.4
Reheated	4.6	92.5	2.9

## Results

### Optical Microscopy

The macroscopic section of the joint in the 0.75-in. plate is shown in Fig. 1A, and the typical microstructures observed in the as-deposited and reheated regions of the weld are shown in Fig. 1B and C. The root and fill passes of the weld metal contain a significant fraction of reheated weld metal,

in Table 2. Within the fill passes, the as-deposited regions had an average hardness of about 285 ( $\pm 6.7$ ) HV<sub>1kgf</sub>, which was comparable to the reheated material with a hardness of 281 ( $\pm 6.0$ ) HV<sub>1kgf</sub>. It should be noted that the capping pass weld metal had a higher hardness of 332 ( $\pm 2.0$ ) HV<sub>1kgf</sub> as a result of the higher cooling rates. Weld metal testing indicated that the yield point was 763 MPa with an ultimate tensile strength of 866 MPa, and elongation to failure of 17.8%, which is consistent with the expected minimum ultimate tensile strength (UTS) of 825 MPa.

### Electron Microscopy and XRD Results

The as-deposited and reheated regions of the weld metal are shown in Fig. 2. There is clearly no basket-weave structure or acicular ferrite present. Instead, bainitic ferrite dominates with a fine packet size in the as-deposited microstructure. The as-deposited regions containing predominantly aligned ferrite were organized into packets that comprised ferrite laths, with an average length of  $7.4 \pm 2.3 \mu\text{m}$  ( $n = 35$ ) and width of  $0.49 \pm 0.18 \mu\text{m}$  ( $n = 54$ ).

The XRD pattern of the bulk weld metal is shown in Fig. 3, and the only peaks that could be indexed consisted of ferrite and retained austenite. Based on the relative intensities of the (220) ferrite peak,  $I_1$ , and the (111) austenite peak,  $I_2$ , the volume fraction of retained austenite RA% can be estimated (Ref. 29) using the following equation:

$$RA\% = \frac{I}{1 + 0.65 \left( \frac{I_1}{I_2} \right)} \quad (1)$$

which indicated that the weld metal contained approximately 2.9% retained austenite.

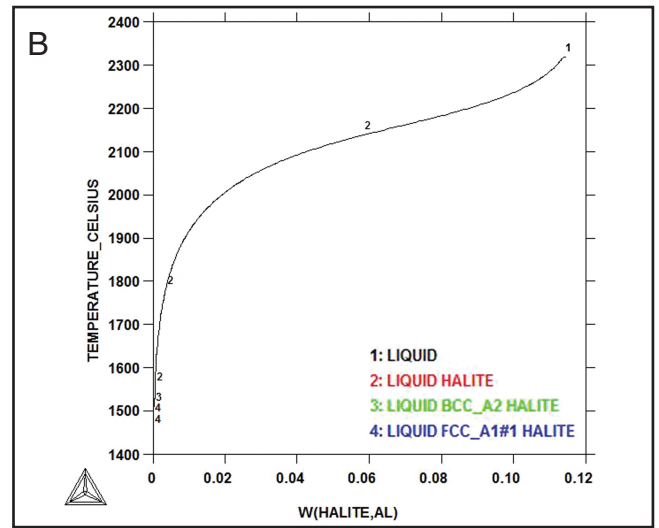
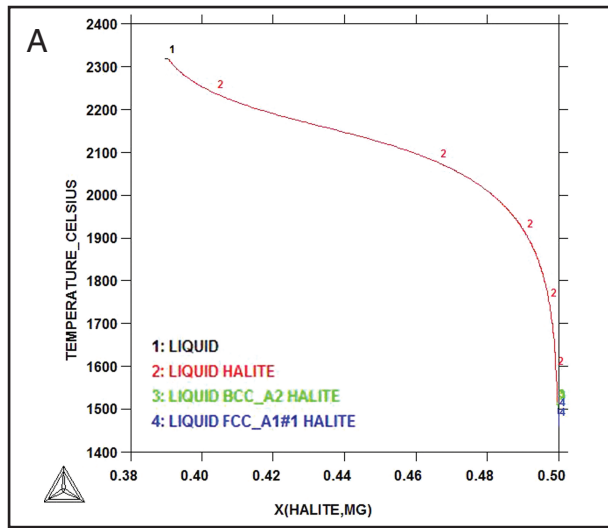


Fig. 4 — Weight fraction of Mg (A) and Al (B) in the halite phase vs. temperature during solidification of the weld metal, calculated using ThermoCalc.



Fig. 5 — SEM micrograph of an Mg- and Al-rich inclusion in weld metal.

### Thermodynamic Analysis

The formation of inclusions in the weld pool was examined by considering the thermodynamic stability of various oxides using *ThermoCalc*, considering the actual weld metal chemistry and the assumptions for a Scheil solidification plot. The results indicated that the equilibrium phases during solidification of the steel first involves

an ionic phase, labeled as ‘Halite’, along with ferrite (BCC\_A1) and retained austenite (FCC\_A1#1). The halite phase consists mainly of MgO, and is included in the *ThermoCalc* TCFE6 database within the Fe-Al-Ca-Cr-Mg-Mn-Ni-Si-Ti-C-O system, with possible substitution of Mg for other elements permitted. In the present work, halite begins to precipitate in the melt at just over 2300°C and is initially aluminum rich, and then devoid of aluminum at lower temperatures <1600°C, and this is followed by solidification of ferrite. The calculated content of magnesium and aluminum in the halite during solidification is shown in Fig. 4, with a balance of oxygen, suggesting it would have (Mg,Al)O chemistry. It should be noted that when magnesium is not included in the chemistry, the calculations suggest that Si<sub>2</sub>O<sub>4</sub>-Al<sub>6</sub>O<sub>9</sub> phase would solidify first in the melt, followed by MnO-Al<sub>2</sub>O<sub>3</sub>, and the halite phase is not formed.

### Inclusion Analysis

Spherical oxide inclusions could be observed in the steel, and measurements indicated they have an average size of 311 ± 120 nm (n = 69). These fine inclusions were found to contain aluminum and magnesium — Fig. 5. Auger electron spectroscopy (AES) was used to map the elemental distribution in these oxides, and a core/shell structure can be observed containing mainly Al oxide in the core, and a shell with Mg oxide — Fig. 6. These observations support the thermodynamic calculations in Fig. 4, which suggest that the inclusions are initially nucleated with a core that is rich in magnesium, aluminum, and oxygen, and then following growth, the outer shell only contains magnesium and oxygen. Some prior research has also shown that halite particles with a MgO stoichiometry are predicted by *ThermoCalc* in steels containing low oxygen content and trace amounts of Mg (Ref. 31) However, to the authors’ knowledge, such Mg-Al-O-rich inclusions have never been reported in weld metal and no correlation could be observed between nucleation of ferrite phases and these inclusions.

The carbides in the steel were also extracted by dissolving the weld metal in a mixture of HCl and HNO<sub>3</sub> acid. The dissolved solution was screened through filter paper in order to capture the solid particles. XRD analysis was used to determine the solid phases recovered following dissolution and filtering. The XRD peaks observed in the residue recovered were identified as ZrC carbide (Ref. 32), and the particles were extracted from the filter paper onto double-sided copper tape for SEM microscopy. This residue is shown in Fig. 7, and consisted mainly of cuboidal particles; however, a small fraction of spherical particles could also be observed, which may correspond with the oxide in-

Table 3 — Instrumented Charpy Impact Testing Measurements

Weld Region	Test Temperature, °C	Dynamic Fracture Toughness J <sub>1d</sub> , kJ/m <sup>2</sup>	Total Energy, J
Top	20	246	94
Top	-18	245	87
Top	-62	280	67
Bottom	20	303	137
Bottom	-18	279	139
Bottom	-62	294	118

clusions observed in Figs. 5 and 6, along with iron-chloride residue, which may have reprecipitated during particle extraction. EDX analysis revealed mainly the presence of oxygen, carbon, iron, and chlorine, with a small fraction of zirconium, magnesium, and aluminum in the extracted residue. Based on the SEM and XRD observations, it would be expected that the cuboidal particles correspond with ZrC, with an average size of  $221 \pm 45$  nm ( $n = 10$ ).

### Charpy Toughness Measurements and Fractography

The impact testing results are shown in Fig. 8. The upper shelf extends to  $-40^\circ\text{C}$ , and the ductile to brittle transition temperature, if defined as the temperature at which toughness is intermediate between the upper and lower shelves, is at  $-60^\circ\text{C}$  or below. The upper shelf value is approximately 130 J, and the lower shelf was never reached, despite tests being conducted down to  $-73^\circ\text{C}$ . The fracture surface of Charpy specimens tested at  $-18^\circ\text{C}$  exhibited mainly a fibrous fracture surface, while those tested at  $-62^\circ\text{C}$  exhibited a combination of fibrous failure and quasi-cleavage fracture, as shown in Fig. 9. Spherical particles could be observed in bottoms of many of the dimples observed in the fibrous fracture surfaces, in addition to a few randomly distributed cuboidal particles, as shown in Fig. 10. The quasi-cleavage fracture surface shown in Fig. 11 had facets with dimensions comparable to the ferrite packed diameters observed by SEM in Fig. 2.

### Instrumented Charpy Testing of Top and Bottom Region of Weld

The top (near the cap) and bottom (near the root) of the welds tested showed significantly different microstructures. The bottom of the weld shows a much higher amount of reheated material, as shown in Fig. 1A, which results in much different balances between FS(A) and FS(NA) microconstituents (higher FS(NA) in reheated material).

The differences in the fracture strength of these two microstructures were investigated using instrumented impact tests. In these tests, the evolution of force during the breaking of the sample is recorded. The resulting curves are illustrated in Fig. 12. These curves provide much richer detail than a report of only total impact energy values. In particular, the dynamic fracture toughness or J-integral value ( $J_{1d}$ ) may also be calculated from the data based on the methodology proposed by Moitra et al. (Ref. 33). In this approach, the standard Charpy sample has a notch and no precrack is present, which requires

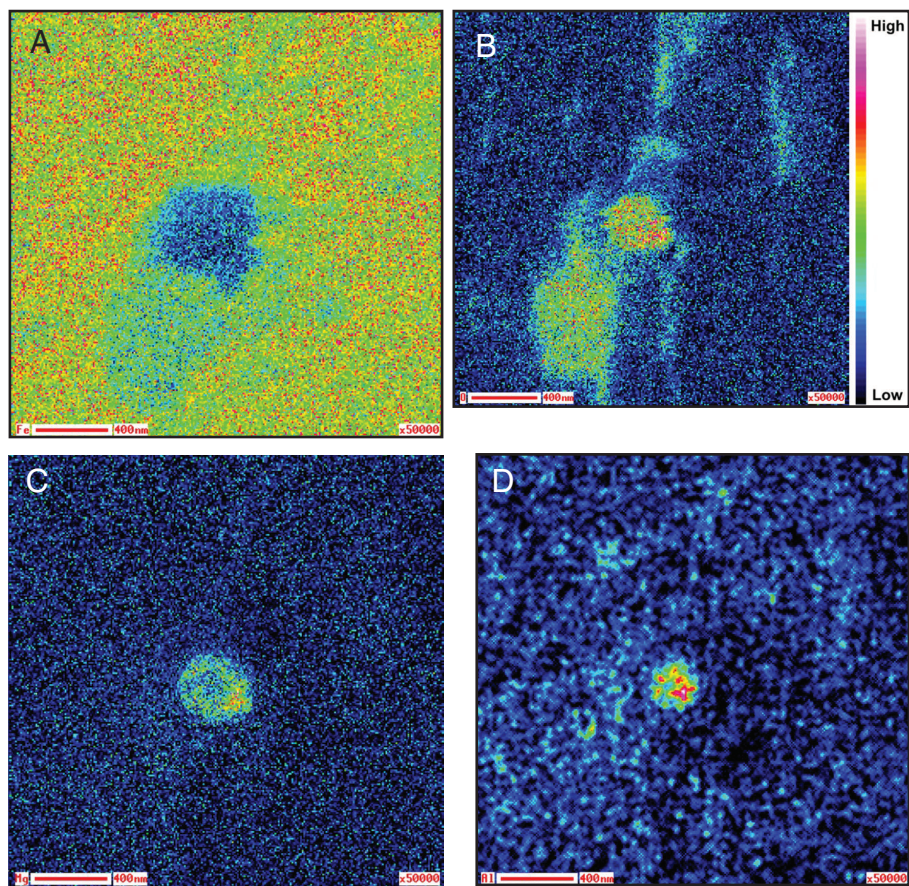


Fig. 6 — AES analysis of element distributions of the Mg- and Al-rich oxide in weld metal, with A — Fe; B — O; C — Mg; D — Al maps shown.

one to estimate when the actual fracture has initiated based on the force-displacement data collected during impact. For this type of specimen, the dynamic fracture toughness is given by:

$$J_{1d} = \eta (E_S)_i B b_o \quad (2)$$

where  $\eta$  is a constant,  $(E_S)_i$  is the energy absorbed up to the crack initiation point, the sample thickness  $B$  is 10 mm, and  $b_o$  is the remaining ligament length of 8 mm. It has been shown that in the case of Charpy impact specimens,  $\eta = 1.45$  (Refs. 33, 34), and that the crack initiation point for ferritic steel specimens can be taken as the point corresponding with  $(P_{MAX} + P_{GY})/2$ , where  $P_{MAX}$  is the maximum load during impact, and  $P_{GY}$  is the general yield load (Ref. 35). In some cases, resonance in the impact tester produced large oscillations in the force output, so the force output data was averaged to remove these oscillations and allow  $P_{MAX}$  and  $P_{GY}$  to be readily determined. The area directly under the force-displacement curve up to the point  $(P_{MAX} + P_{GY})/2$  was then quantified to directly measure  $(E_S)_i$ .

The measured values for the impact performance of the top and bottom regions of the weld are summarized in Table

3. The  $J_{1d}$  and the total impact energy are similar for both regions of the weld (slightly higher for the bottom region, with the difference more marked at lower temperatures). The fracture surfaces are also comparable, with slightly finer features (average size of dimples) in the bottom. The similarity in fracture toughness and fracture surface between the top and the bottom of the weld, despite having such different balances of FS(A) and FS(NA) is consistent with a fracture mechanism dominated by inclusions and carbides, which are stable during reheating and are expected to have a similar distribution in the top and bottom of the weld. In a mechanism dominated by carbides and inclusions, smaller inclusions result in higher toughness values, and the small size of the inclusions and carbides observed here (all below  $0.5 \mu\text{m}$ ) are an important factor in the high-impact values observed.

### Discussion

In prior investigations, Koseki and Thewlis have shown that toughness and strength degrades when the weld metal Al/O ratio exceeds 1.0 (Ref. 4), since these will promote a spinel structure that does not favor acicular ferrite nucleation (Ref.

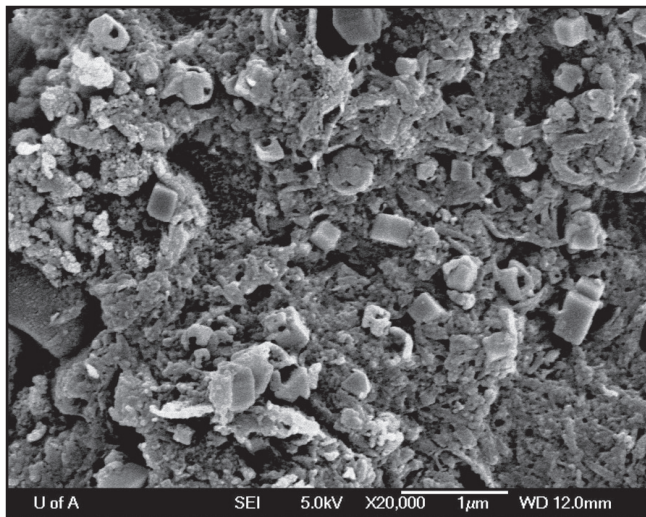


Fig. 7 — SEM micrograph of particles extracted from the weld metal following dissolution in acid.

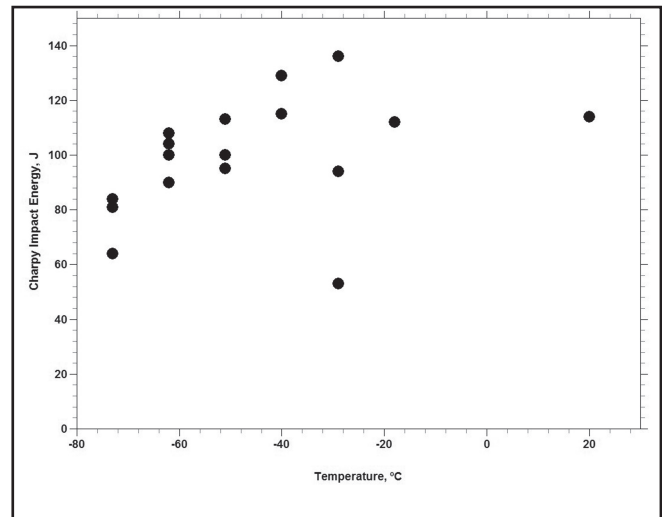


Fig. 8 — Charpy impact energy values for material extracted from the middle region of the fusion zone.

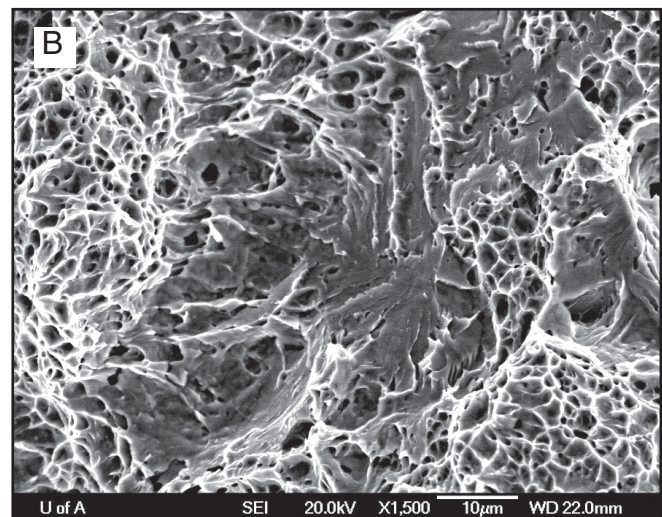
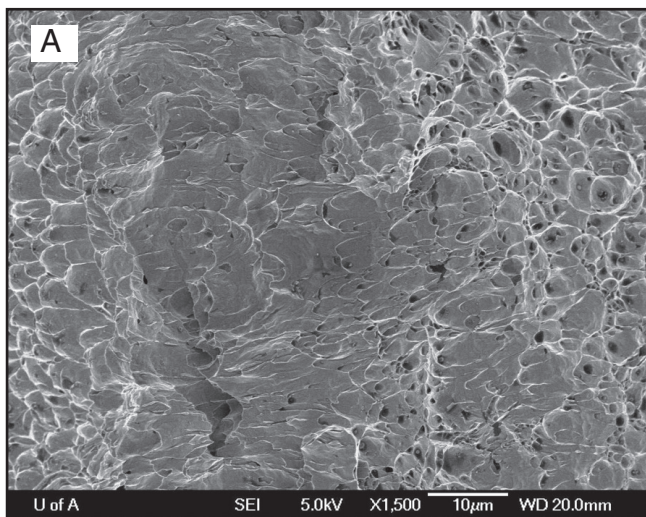


Fig. 9 — Fracture surfaces from central region of the Charpy sample for tests. A —  $-18^{\circ}\text{C}$ ; B —  $-62^{\circ}\text{C}$ .

36). However, this ideal Al/O ratio is based on the fraction of acicular ferrite being maximized, as long as titanium is present (Ref. 37). Since the Al/O ratio was extremely high and there was negligible titanium content, no acicular ferrite formed in the weld metal.

Precipitate particles with dimensions  $>1\ \mu\text{m}$  could not be observed in the inclusions extracted from the weld metal by dissolution, or on the fracture surfaces, suggesting that the presence of submicron sized (Mg, Al)O particles may have suppressed the coarsening of oxide inclusions. The oxygen content measured in the weld metal (120 ppm) is within the range observed for gas metal arc welds; however, the particularly low nitrogen content (64 ppm) is attributed to the use of  $\text{CO}_2$  shielding gas along with the high aluminum content (0.557 wt-%). For any given level of oxygen content, a transition

from a small number of large inclusions to a large number of fine inclusions will result in lower room temperature fracture energy values since the number of initiation points for fibrous fracture will increase (Ref. 38), particularly if decohesion has already occurred at the particle interface upon cooling of the weld metal. In the case of cleavage fracture, fracture stress increases dramatically with decreasing inclusion size, particularly those  $<0.5\ \mu\text{m}$  in diameter (Ref. 39), as in the case of the weld metal examined here. Further analysis could not directly correlate the size and spacing of the inclusions to any other microstructural features.

It is interesting to note a shelled inclusion structure similar to the one observed in this work (but without Mg) was observed in a prior study of flux cored consumables containing Ti and Zr by Narayan et al. (Ref. 40). They showed that the for-

mation of a core/shell structure prevents coarsening and agglomeration of inclusions by “capping” the aluminum oxide particles and suppressing their growth. In that study, a much higher fraction of nitrogen (0.018 to 0.020 wt-%) was present in the weld metal, promoting a shell of (Zr,Ti)N to cap the inclusions. In the present work, it appears that magnesium may have a similar effect in suppressing the coarsening or agglomeration of the oxides in the liquid weld metal, as suggested by the thermodynamic calculations in Fig. 4.

The amount of retained austenite measured (2.9%) is comparable to 9.4% measured using the same technique previously in steel welds containing 9 wt-% Ni (Ref. 41), where no peaks corresponding with martensite could be detected (Ref. 42). However, this does not necessarily indicate that martensite was absent since the low carbon content of the weld metal

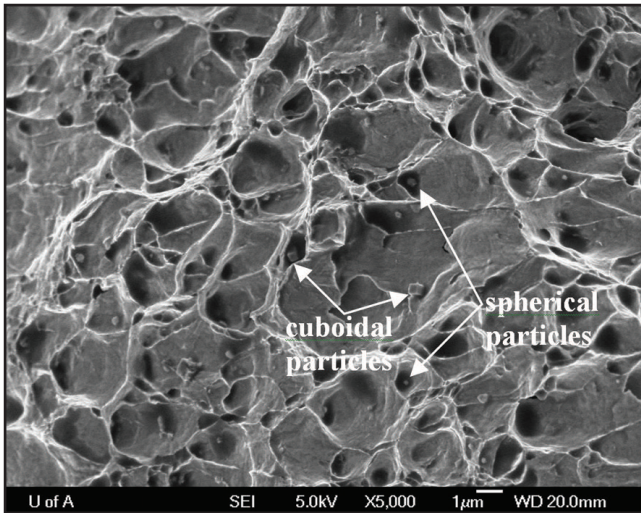


Fig. 10 — Particles observed on fracture surface of Charpy sample tested at  $-18^{\circ}\text{C}$ .

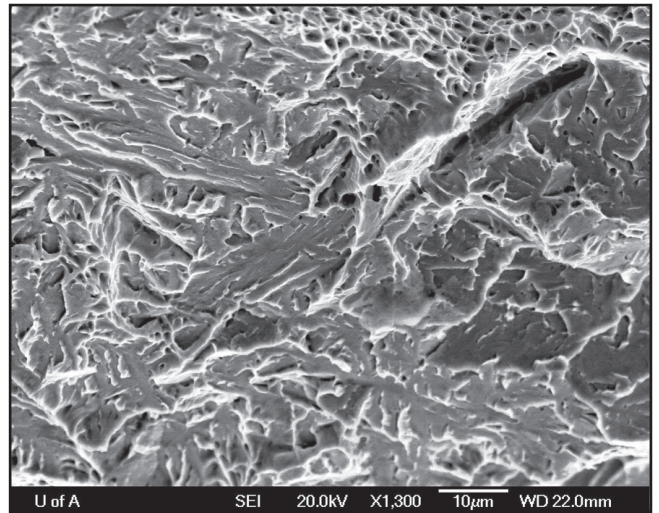


Fig. 11 — Facets observed on the quasi-cleavage fracture surface of Charpy sample tested at  $-62^{\circ}\text{C}$ .

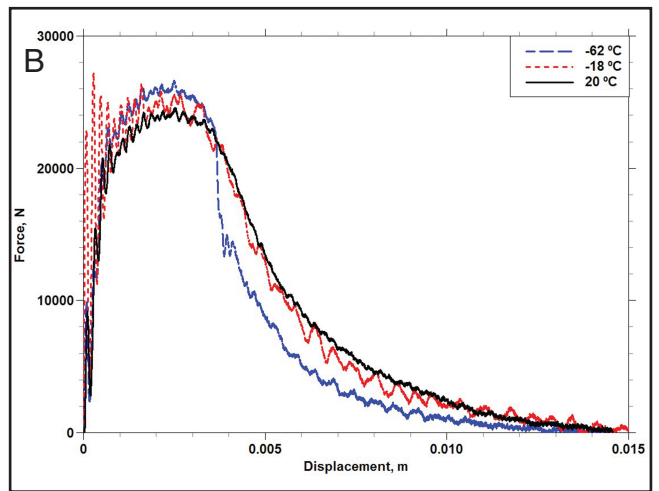
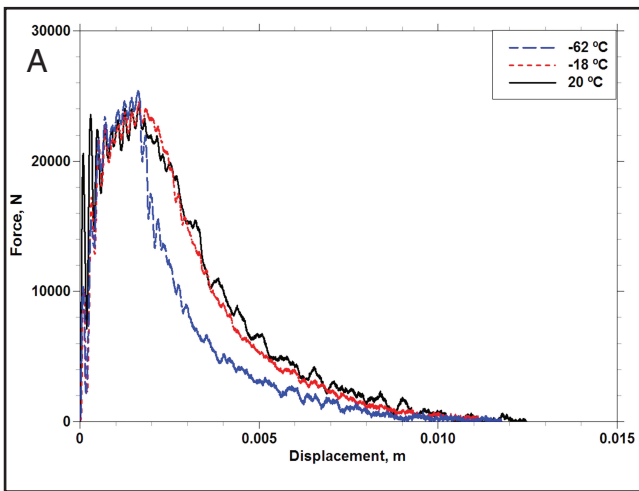


Fig. 12 — Instrumented Charpy impact data showing force and displacement during impact from the A — Top region of weld; B — bottom region.

would minimize lattice strains, making it difficult to detect martensite via XRD. Regardless, the presence of a significant fraction of austenite may be beneficial during fracture, and the nickel content (3.51%) of the weld metal likely provides an austenite stabilization effect (Refs. 41, 43). The addition of Ni to weld metal has long been known to improve low-temperature toughness of weld metals, particularly below  $-30^{\circ}\text{C}$  (Refs. 44–46). For example, more than a  $100^{\circ}\text{C}$  decrease in the ductile to brittle transition temperature can be achieved when only 3.5% nickel is added to steel (Ref. 47).

The Charpy toughness values and impact transition temperature achieved in Fig. 8 are comparable to those observed in a 9%Ni steel, despite using a much lower nickel content (Ref. 41). Reducing the fraction of interstitials, in addition to the presence of nickel in solution is also known to increase the cleavage fracture strength and lower the brittle transition temperature dra-

matically. The premise is that nickel improves the cohesive strength of the ferrite lattice itself, which contributes to the enhanced fracture properties (Ref. 48). The present work suggests that an additional enhancement may occur due to a change in the distribution of microconstituents as well, since nickel is an austenite stabilizer. For example, when MA phase does not contain martensite but rather is dominated by austenite, this may also enhance toughness properties (Ref. 49).

The high fracture toughness values obtained at low temperatures are also promoted by the fine-grained ferrite microstructures produced in the welds in combination with small-diameter oxide inclusions. The fine ferrite sizes with fewer aligned microstructures in reheated zones contributed to the higher fracture energy values. Aligned ferrite grains are typically separated by boundaries with low-angle misorientation (Ref. 50), and do not promote crack deviation during cleavage frac-

ture. When the width of the ferrite laths or size of the packets are reduced (as shown in Figs. 1 and 2), and few aligned carbides are present, the cleavage fracture stress increases dramatically (Ref. 51). Since the FS(A) microconstituents that dominate the upper portion of the weld exhibit a fine packet size, this contributed to the fracture toughness in the top regions of the weld (containing mostly the as-deposited material), reducing the unit crack path during fracture (Refs. 23, 52). Both  $J_{1d}$  and the total impact energy are slightly higher for the bottom region of the weld, and this trend is explained by increased fraction of reheated material with a microstructure that contains a lower fraction of aligned ferrite/carbide phases. The difference in toughness between top and bottom is more pronounced at lower temperatures, where cleavage fracture dominates and the finer microstructures with fewer aligned ferrite microconstituents result in higher fracture energies.

It is particularly interesting to note that the fine spherical Mg-Al-O-based inclusions were formed in the presence of 300 ppm of Mg in the weld metal. There has been limited discussion in the literature on the application of Mg as an alloying element in steels; however, it has been noted to produce nitride and oxide precipitates, which may be useful in refining the grain structure in the heat-affected zone (Ref. 53). The use of MgO in welding flux is common, due to the strong deoxidizing role of Mg in the weld metal (Ref. 54), although the concentration of Mg in weld metal is seldom ever reported due to its low solubility in steel. To the authors' knowledge, this work represents the first time that Mg has been observed to play a significant role in the structure of fine oxides in a weld metal, as indicated by the AES observations in Fig. 6 and the thermodynamic modeling in Fig. 4. Since the chemistry and microstructural features contributing to the properties of the weld metal were heavily influenced by the flux used here (Ref. 27), it is worth examining how this can be optimized further in consumables for other processes.

## Conclusions

Fine Mg-bearing inclusions with a core/shell structure have been observed in a carbon steel weld metal. Flux cored arc welding was used to produce a weld metal that contained primarily bainitic ferrite with a fine packet size in the as-deposited metal and mainly nonaligned ferrite in the reheated zones. Spherical inclusions with an average diameter of 311 nm were observed with a shelled structure that was mainly rich in aluminum, magnesium, and oxygen in the core, vs. magnesium and oxygen in the outer shell, which was suggested to be halite based on thermodynamic calculations for the weld metal chemistry. The combination of a fine inclusion size, nickel in solution, a low content of interstitials (such as [O] and [N]), along with a fine ferrite packet size, were suggested to provide an excellent combination of toughness and strength. Instrumented impact testing showed the slight increase in grain refinement in reheated zones around the root of the weld improved impact properties, although fracture initiation energies were comparable to the top of the weld.

## Acknowledgments

Financial support was provided from Hobart Brothers and Natural Sciences and Engineering Research Council of Canada (NSERC). Discussions with Mario Amata of Hobart Brothers, and Graham Thewlis are also greatly appreciated.

## References

- Mori, N., Homma, H., Ohkita, S., and Wakabayashi, M. 1981. *J. Jpn. Weld. Soc.* 50: 175–181.
- Abson, D. J., and Pargeter, R. J. 1986. *Int. Met. Rev.* 31(4): 141–194.
- Ferrante, M., and Farrah, R. A. 1982. *Journal of Materials Science* 17: 3293–3298.
- Koseki, T., and Thewlis, G. 2005. *Mater. Sci. Tech.-Lond.* 21(8): 867–879.
- Ohkita, S., and Horii, Y. 1995. *Isij. Int.* 35(10): 1170–1182.
- Gourgues, A. F., Flower, H. M., and Lindley, T. C. 2000. *Mater. Sci. Tech.-Lond.* 16(1): 26–40.
- Gregg, J. M., and Bhadeshia, H. K. D. H. 1994. *Acta Metall Mater* 42(10): 3321–30.
- Kou, S. 2003. *Welding Metallurgy*. 2nd ed. Wiley-Interscience, Hoboken, N.J.
- Koseki, T., Ohkita, S., and Yurioka, N. 1997. *Sci. Technol. Weld. Joi.* 2(2): 65–9.
- Ashby, M. F., and Easterling, K. E. 1982. *Acta Metallurgica*. 30(11): 1969–78.
- Fleck, N. A., Grong, O., Edwards, G. R., and Matlock, D. K. 1986. *Welding Journal* 65(5): 113-s to 121-s.
- Edwards, G. R., and Liu, S. 1990. *Proceedings of the first US-Japan Symposium on Advanced Welding Metallurgy*. AWA/JWS/JWES: San Francisco, Calif., and Yokohama, Japan. pp. 213–292.
- Bhadeshia, H. K. D. H., and Christian, J. W. 1990. *Metall. Trans. A* 21(4): 767–797.
- Widgery, D. J., and Knott, J. F. 1978. *Met. Sci.* 12(1): 8–11.
- Tweed, J. H., and Knott, J. F. 1983. *Met. Sci.* 17(2): 45–54.
- S. Terashima, S., and Bhadeshia, H. K. D. H. 2006. *Sci. Technol. Weld. Joi.* 11(5): 509–516.
- Babu, S. S. 2004. *Current Opinion in Solid State and Materials Science* 8: 267–278.
- Shanmugam, S., Ramiseti, N. K., Misra, R. D. K., Hartmann, J., and Jansto, S. G. 2008. *Mat. Sci. Eng. a-Struct.* 478(1-2): 26–37.
- de Rissone, N. M. R., Bott, I. D., de Vedia, L. A., and Surian, E. S. 2003. *Sci. Technol. Weld. Joi.* 8(2): 113–122.
- Steel, A. C. 1972. *Weld. Res. Intl.* (3): 37–76.
- Ahlblom, B. 1984. IHW Doc. IXJ-81-84.
- Ito, Y., and Nakashin, M. 1976. *Sumitomo Search* 15(42–62): 42.
- Ito, Y., Nakashin, M., and Komizo, Y. 1982. *Met. Contr.* 14(9): 472–478.
- Terashima, H., and Tsuboi, J. 1982. *Met. Constr.* 14(12): 648–654.
- Judson, P., and McKeown, D. 1983. *Off-shore Welded Structures*. 1983. The Welding Institute: Abington, UK. Paper 3.
- Lancaster, J. F. 1993. *Metallurgy of Welding*. 5th ed., Chapman & Hall, London, New York.
- Amata, M., and Bundy, J. C. 2008. Aluminum Deoxidizing Welding Wire, Intl. Patent No. US2008/0272100 A1, United States, Illinois Tool Works, Inc.
- Quintana, M. A., McLane, J., Babu, S. S., and David, S. A. 2001. *Welding Journal* 80(4): 98-s to 105-s.
- Thewlis, G. 2004. *Mater. Sci. Tech.-Lond.* 20(2): 143–160.
- Zhang, H., Zhang, L., Cheng, X. L., and Bai, B. Z. 2010. *Acta. Mater.* 58(18): 6173–6180.
- Bergman, O., and Nyborg, L. 2010. *Powder Metallurgy Progress* 10(1): 1–19.
- Song, M. S., Huang, B., Zhang, M. X., and Li, J. G. 2008. *Cryst. Growth* 310(18): 4290–4294.
- Moitra, A., Sreenivasan, P. R., Parameswaran, P., and Mannan, S. L. 2002. *Mater. Sci. Techn.-Lond.* 18: 1195–2000.
- Sreenivasan, P. R., and Mannan, S. L. 2000. *Int. J. Fracture* 101(3): 215–228.
- Ghoneim, M. M., and Hammad, F. H. 1992. *J. Nucl. Mater.* 186(2): 196–202.
- Takada, A., Terasaki, H., and Komizo, Y. 2013. *Sci. Technol. Weld. Joi.* 18(2): 91–97.
- Evans, G. M. 1991. *Oerlikon Schweissmitt* 49(125): 22–33.
- Lalam, S. H., Bhadeshia, H. K. D. H., and MacKay, D. J. C. 2000. *Sci. Technol. Weld. Joi.* 5(3): 149–160.
- Bose, W. W., Carvalho, A. L. M., and Bowen, R. 2007. *Mat. Sci. Eng. a-Struct.* 452: 401–410.
- Narayanan, B. K., Kovarik, L., Sarosi, P. M., Quintana, M. A., and Mills, M. J. 2010. *Acta. Mater.* 58(3): 781–791.
- Nippes, E. F., and Balaguer, J. P. 1986. *Welding Journal* 65(9): 237-s to 243-s.
- Cheary, R. W., and Ying, M. S. 2000. *Journal of Materials Science* 35(5): 1105–1113.
- Shiue, R. K., Lan, K. C., and Chen, C. 2000. *Mat. Sci. Eng. a-Struct.* 287(1): 10–6.
- Morigaki, O., Tanigaki, T., Kuwabara, M., Fubayashi, K., and Otawa, M. 1975. IHW, 1975. Doc. II 746-775.
- Abson, D. J., and Dolby, R. E. 1980. *Weld. Inst. Res. Bull.* 21(4): 100–103.
- Abson, D. J., and Dolby, R. E. 1980. IHW Doc. IXJ 29-80.
- United States Steel Corp. and McGannon, H. E. 1971. *The Making, Shaping and Treating of Steel*. 9th ed. United States Steel, Pittsburgh, Pa.
- Leslie, W. C. 1972. *Metall. Trans.* 3(1): 5–26.
- Lambert, A., Drillet, J., Gourgues, A. F., Sturel, T., and Pineau, A. 2000. *Sci. Technol. Weld. Joi.* 5(3): 168–173.
- Edmonds, D. V., and Cochrane, R. C. 1990. *Metall. Trans. A* 21(6): 1527–1540.
- Hahn, G. T. 1984. *Metall Trans A* 15(6): 947–959.
- Ito, Y., and Nakashin, M. 1979. *Sumitomo Search* 21: 52–67.
- Ohkita, S., and Oikawa, H. 2007. Nippon Steel Technical Report 95(2): 1–10.
- Surian, E. S., and de Rissone, N. M. R. 1999. *Sci. Technol. Weld. Joi.* 4(3): 133–142.